The Astronomical Journal, 169:4 (10pp), 2025 January https://doi.org/10.3847/1538-3881/ad8ec1

Origins of Super Jupiters: TOI-2145b has a Moderately Eccentric and Nearly Aligned Orbit

Jiayin Dong[1,2,19], Ashley Chontos[3,20], George Zhou[4], Gudmundur Stefansson[5], Songhu Wang[6], Chelsea X. Huang[4], Arvind F. Gupta[7,21], Samuel Halverson[8], Shubham Kanodia[9,22], Jacob K. Luhn[8,10,23], Suvrath Mahadevan[11,12,24], Andrew Monson[13], Jaime A. Alvarado-Montes[14,15], Joe P. Ninan[16], Paul Robertson[10,25], Arpita Roy[17], Christian Schwab[14,15], and Jason T. Wright[11,12,18]

[1] Center for Computational Astrophysics, Flatiron Institute, 162 Fifth Avenue, New York, NY 10010, USA; jdong@flatironinstitute.org
[2] Department of Astronomy, University of Illinois at Urbana-Champaign, Urbana, IL 61801, USA
[3] Department of Astrophysical Sciences, Princeton University, 4 Ivy Lane, Princeton, NJ 08540, USA
[4] University of Southern Queensland, Centre for Astrophysics, West Street, Toowoomba, QLD 4350, Australia
[5] Anton Pannekoek Institute for Astronomy, 904 Science Park, University of Amsterdam, Amsterdam, 1098 XH, The Netherlands
[6] Department of Astronomy, Indiana University, Bloomington, IN 47405, USA
[7] U.S. National Science Foundation National Optical-Infrared Astronomy Research Laboratory, 950 N. Cherry Avenue, Tucson, AZ 85719, USA
[8] Jet Propulsion Laboratory, California Institute of Technology, 4800 Oak Grove Drive, Pasadena, CA 91109, USA
[9] Carnegie Science Earth and Planets Laboratory, 5241 Broad Branch Road, NW, Washington, DC 20015, USA
[10] Department of Physics & Astronomy, The University of California, Irvine, Irvine, CA 92697, USA
[11] Department of Astronomy & Astrophysics, 525 Davey Laboratory, Penn State, University Park, PA 16802, USA
[12] Center for Exoplanets and Habitable Worlds, 525 Davey Laboratory, Penn State, University Park, PA 16802, USA
[13] Steward Observatory, University of Arizona, 933 N. Cherry Avenue, Tucson, AZ 85721, USA
[14] School of Mathematical and Physical Sciences, Macquarie University, Balaclava Road, North Ryde, NSW 2109, Australia
[15] The Macquarie University Astrophysics and Space Technologies Research Centre, Macquarie University, Balaclava Road, North Ryde, NSW 2109, Australia
[16] Department of Astronomy and Astrophysics, Tata Institute of Fundamental Research, Homi Bhabha Road, Colaba, Mumbai 400005, India
[17] Astrophysics & Space Institute, Schmidt Sciences, New York, NY 10011, USA
[18] Penn State Extraterrestrial Intelligence Center, 525 Davey Laboratory, Penn State, University Park, PA 16802, USA
Received 2024 June 24; revised 2024 October 12; accepted 2024 November 1; published 2024 December 4

Abstract

Super Jupiters are giant planets with several Jupiter masses. It remains an open question whether these planets originate with such high masses or grow through collisions. Previous work demonstrates that warm super Jupiters tend to have more eccentric orbits compared to regular-mass warm Jupiters. This correlation between mass and eccentricity may indicate that planet–planet interactions significantly influence the warm giant planet demographics. Here, we conducted a detailed characterization of a warm super Jupiter, TOI-2145b. This analysis utilized previous observations from Transiting Exoplanet Survey Satellite and Keck/High Resolution Echelle Spectrometer, enhanced by new Rossiter–McLaughlin effect data from the NEID spectrometer on the 3.5 m WIYN Telescope. TOI-2145b is a $5.68^{+0.37}_{-0.34}\,M_{\rm Jup}$ planet on a moderate eccentricity ($e = 0.214^{+0.014}_{-0.014}$), 10.26 day orbit, orbiting an evolved A-star. We constrain the projected stellar obliquity to be $\lambda = 6.8^{+2.9}_{-3.8}{}^{\circ}$ from two NEID observations. Our *N*-body simulations suggest that the formation of super Jupiter TOI-2145b could involve either of two scenarios: a high initial mass or growth via collisions. On a population level, however, the collision scenario can better describe the mass–eccentricity distribution of observed warm Jupiters.

Unified Astronomy Thesaurus concepts: Exoplanets (498); Exoplanet formation (492); Transits (1711)

1. Introduction

It has long been recognized that a positive correlation between planetary mass and orbital eccentricity exists among radial velocity (RV)–discovered giant planets (R. P. Butler et al. 2006; J. T. Wright et al. 2009). These giant planets have orbital periods ranging from a few days to several thousand days and projected mass ($M_p \sin i$) from roughly 0.1 to 10 $M_{\rm Jup}$. This positive mass-eccentricity correlation has been interpreted as a result of planet–planet interactions, such as scatterings and collisions (e.g., S. Chatterjee et al. 2008; E. B. Ford & F. A. Rasio 2008; M. Jurić & S. Tremaine 2008; R. Frelikh et al. 2019).

Recently, a similar trend has been reported in the population of transiting warm Jupiters (A. F. Gupta et al. 2024). Close-in giant planets with masses ranging from 0.3 to 15 $M_{\rm Jup}$ and orbital periods between 10 and 365 days exhibit a mass-dependent eccentricity distribution. Unlike many planets discovered via RV, these transiting giant planets do not suffer from the mass degeneracy due to the unknown orbital inclination angle. Warm Jupiters less massive than 2 $M_{\rm Jup}$ tend to have circular or low-eccentricity orbits, while those more massive than 2 $M_{\rm Jup}$—i.e., super Jupiters—exhibit a broad range of eccentricities. This mass–eccentricity dependence likely explains the bimodal eccentricity distribution observed in warm Jupiters (J. Dong et al. 2021), where the observed low-e component

[19] Flatiron Research Fellow.
[20] Henry Norris Russell Fellow.
[21] NOIRLab Postdoctoral Fellow.
[22] Carnegie EPL Fellow.
[23] NASA Postdoctoral Program Fellow.
[24] NEID Principal Investigator.
[25] NEID Instrument Team Project Scientist.

represents the low-mass warm Jupiters, while the high-e component represents the warm super Jupiters.

Planet–planet interactions likely play a role in shaping the mass and eccentricity distribution of warm Jupiters, shedding light on their origins. Among these, the formation of super Jupiters is particularly interesting. These massive planets can either form through collisions between multiple lower-mass giant planets, resulting in low eccentricity and mutual inclinations, or they may be born massive, with their eccentricity and inclination further excited by companions. It is also unclear whether the origin of super Jupiters depends on stellar properties. To better understand this feature, we conduct a detailed characterization of a warm super Jupiter, TOI-2145b. The planet was first discovered and had its orbital properties confirmed by J. E. Rodriguez et al. (2023) and later had its properties refined by A. Chontos et al. (2024). TOI-2145b is a 10.3 day period, 5.7 Jupiter-mass planet orbiting a retired A-star ($M_\star = 1.71 \pm 0.04\,M_\odot$, $\log g = 3.79 \pm 0.02$). The planet has a moderate orbital eccentricity of 0.22 but unknown stellar obliquity.

The underlying assumption of planet–planet interactions as the cause of the observed mass–eccentricity trend is that dynamical interactions primarily occur at the semimajor axes of the planets observed today. Whether giant planets migrated inward or formed in situ, postformation dynamical interactions shape the observed trend (D.-H. Wu et al. 2023). Under such assumptions, planet–planet interactions could excite mutual inclinations between planets, but not significantly so ($i_{\rm mutual} < 40°$; K. R. Anderson et al. 2020). This is consistent with the trend of low stellar obliquity observed in the warm Jupiter population around single stars (e.g., J. Dong et al. 2022; M. Rice et al. 2022; B. T. Radzom et al. 2024; X.-Y. Wang et al. 2024). Some warm Jupiters, such as TOI-1859b (J. Dong et al. 2023), are found in misaligned orbits; however, their host stars often have distant stellar companions, with projected distances around 2400 au in this case. The impact of stellar companions on planet formation remains unclear.

In this work, we present the Rossiter–McLaughlin (RM) effect measurements of TOI-2145b (HIP 86040) using the high-resolution (HR) NEID spectrograph. In Section 2, we summarize previous Transiting Exoplanet Survey Satellite (TESS) and High Resolution Echelle Spectrometer (HIRES) observations. In Sections 3 and 4, we model and present the stellar and planetary properties of TOI-2145b, respectively, combining the TESS transits, HIRES RV, and NEID RM-effect and Doppler Tomography (DT) signals. We also search for external companions of TOI-2145b using Gaia and Hipparcos astrometry. Lastly, in Section 5, we discuss the properties of the TOI-2145 system and its implications for warm Jupiter origins.

2. Observations

2.1. Summary of Previous Observations

The planet TOI-2145b was detected by TESS (G. R. Ricker et al. 2014). J. E. Rodriguez et al. (2023) first discovered and confirmed its planetary nature using ground-based photometry from the TESS Follow-up Observing Program (K. Collins et al. 2018), HR adaptive optics imaging with the PHARO instrument (T. L. Hayward et al. 2001) on the Palomar 200 inch telescope and ShARCS on the Shane 3 m telescope at Lick Observatory, and HR spectroscopy with the Tillinghast Reflector Echelle Spectrograph (Fűrész 2008) on the 1.5 m Tillinghast Reflector at the Fred Lawrence Whipple Observatory, as well as the MINERVA North telescope array and KiwiSpec Spectrograph (J. J. Swift et al. 2015; M. L. Wilson et al. 2019) at Whipple Observatory. The planet's mass and orbit have been constrained. Later, A. Chontos et al. (2024) refined the planet's mass and orbital parameters using the HIRES Spectrograph (S. S. Vogt et al. 1994) on the Keck 10 m telescope on Maunakea, Hawaii.

Here, we briefly summarize the observations used in our modeling. The star has been observed in six sectors of TESS—Sectors 25, 26, 40, 52, 53, and 79. As this manuscript was being prepared, the Quick Look Pipeline (QLP; C. X. Huang et al. 2020a, 2020b) reduced light curves cover Sectors 25, 26, 40, 52, and 53. Notably, the observing cadence decreases from 30 minutes in Sectors 25 and 26 to 10 minutes in Sectors 40, 52, and 53. The Science Processing Operations Center (SPOC; J. M. Jenkins et al. 2016) reduced light curves are available for Sectors 26, 40, 52, 53, and 79, all with an observing cadence of 2 minutes. Additionally, 20 s cadence data is available for Sector 79. We use the 2 minute SPOC light curves from Sectors 26, 40, 52, 53, and 79, along with the QLP light curves from Sector 25, for the joint fit. Forty HIRES spectra were taken from 2020 August 25 to 2022 May 13, spanning 1.7 yr (A. Chontos et al. 2024). The median HIRES RV uncertainty is 5.2 m s^{-1}, although this number could be underestimated given the star's large $v \sin i_\star$. The HIRES RVs are used for the joint fit with a treatment of the underestimated RV uncertainties.

2.2. Transit Spectroscopic Observation

Two transit spectroscopy observations were taken by the NEID spectrograph (S. Halverson et al. 2016; C. Schwab et al. 2016) on the WIYN 3.5 m telescope at the Kitt Peak National Observatory in Arizona, USA. The NEID spectrograph is a highly stabilized (G. Stefansson et al. 2016; P. Robertson et al. 2019), fiber-fed (S. Kanodia et al. 2018, 2023) spectrograph with a resolving power of $R \approx 110{,}000$ in HR mode and has wavelength coverage from 380 to 930 nm. The first NEID RM-effect visit occurred on 2023 May 26. The observation began at 03:10 UT and lasted 6.3 hr. We obtained 35 spectra, each with a 10 minute exposure time, in HR mode, covering approximately 69% of the transit. The second NEID visit took place on 2023 July 6. The observation started at 02:30 UT and lasted 7.5 hr. We obtained 41 spectra, each with a 10 minute exposure time, in HR mode, covering approximately 77% of the transit.

The NEID data reduction has been performed using three different pipelines: the standard NEID Data Reduction Pipeline v1.3.0 (NEID-DRP), the SERVAL Pipeline (M. Zechmeister et al. 2018; G. Stefànsson et al. 2022), and DT (A. Collier Cameron et al. 2010). The NEID-DRP pipeline utilizes the cross-correlation function (CCF) technique to extract the radial velocities. Due to a minor bug in the NEID-DRP that causes the computed RV error bars to be systematically overestimated for certain targets that have significantly discrepant systemic velocities relative to literature values, we recalculated the RV errors independently using the DRP-derived CCFs using standard techniques (I. Boisse et al. 2010). The median NEID-DRP RV uncertainties are 15.4 and 11.9 m s^{-1} for the first and second visits, respectively. The SERVAL pipeline initially builds a stellar template from the NEID observations and uses least-square fitting to extract the radial velocities. The median RV uncertainties out of the SERVAL pipeline are

9.5 and 7.0 m s^{-1} for the first and second visits, respectively. Lastly, DT models the line profile variations induced by the transiting shadow of the planet. The line profiles are derived via a least-square deconvolution (J.-F. Donati et al. 1997) of each observation against a nonrotating synthetic template generated from the ATLAS9 model atmospheres (F. Castelli & R. L. Kurucz 2004). An average line profile is then removed from each observation, and the residuals are modeled for the planetary transit signature.

3. Stellar Properties

We derive the stellar parameters following the procedures described in Section 4 of A. Chontos et al. (2024). We first use `SpecMatch-Synth` (E. A. Petigura 2015) to derive the stellar effective temperature ($T_{\rm eff}$), metallicity ([Fe/H]), and surface gravity ($\log g$) of the star. We then model the spectral energy distribution (SED) and the MESA Isochrones and Stellar Tracks (J. Choi et al. 2016; A. Dotter 2016) to derive the age, mass, and radius of the star using `isoclassify` (D. Huber et al. 2017). The stellar parameters $T_{\rm eff}$ and [Fe/H] from `SpecMatch` are used as inputs for the model. We include the Johnson B and V magnitudes from the APASS catalog (A. A. Henden et al. 2015); Two Micron All Sky Survey; J, H, and K_s magnitudes (M. F. Skrutskie et al. 2006); and the Gaia DR3 G, R_p, and B_p magnitudes (Gaia Collaboration et al. 2021) to fit the SED. The Gaia DR3 parallax (Gaia Collaboration et al. 2021) is used to determine the distance to the star. The results are summarized in Table 1.

The star has four blocks of TESS data, separated by 1 or 2 yr gaps. To avoid the dominance of the window function in the periodogram for the entire data set, we calculate the periodogram of the light curve piece by piece. Interestingly, the Sectors 25–26 TESS data from 2019 show a periodicity of 5.9 days, whereas Sector 40 in 2020 shows 7.0 days, Sectors 52–53 in 2021 show 5.1 days, and Sector 79 in 2024 shows 3.4 days. The period detected in Sector 79 is shorter than those in the other sectors, which might indicate that it is an alias of 6.8 days. We attribute the lack of consistency in the star's periodicity to its multiple spot complexes. The rotation periods between 5 and 7 days correspond to an equatorial velocity of 20–28 km s^{-1}. As a sanity check, this velocity is above the projected rotational velocity of $\sim$18 km s^{-1}, and the deviation may indicate a stellar inclination apart from 90°. Although the star is evolved, existing TESS data did not detect the oscillation modes of TOI-2145. According to the scaling relation for the oscillation frequency $\nu_{\rm max} = 3100\ \mu{\rm Hz}\ (M/M_\odot)(R/R_\odot)^{-2}(T_{\rm eff}/T_{\rm eff,\odot})^{-0.5}$ (W. J. Chaplin et al. 2019), TOI-2145 should oscillate at $\sim$58 cycles per day, a signal that is not detected in the TESS data.

4. Planet Properties

4.1. TTV Modeling

Since both of our RM-effect measurements captured only a partial transit of TOI-2145b, understanding the transit-timing variation (TTV) properties of the planet is crucial for robust stellar obliquity inference. We modeled the TESS transits, treating each transit's midtransit time as a free parameter. We then fitted a linear line to the midtransit times, deriving the orbital period, one reference transit epoch, and TTV signals. Benefiting from multiple sectors of TESS observations over 4 yr, we modeled 15 transits of TOI-2145b over this period. The results are shown in Figure 1. The scatter in TTVs is less than 5 minutes, with the median midtransit time uncertainty of about 3.7 minutes. No obvious TTV patterns have been detected in existing TESS observations. We derive the orbital period $P = 10.261129 \pm 0.000009$ in days and reference transit epoch $T_C = 1982.49664 \pm 0.00067$ in BJD−2457000.

Because of the lack of TTVs, in the global modeling to be discussed in the next section, we model P and T_C without individually modeling each midtransit time. The derived orbital period and reference transit epoch well agree with those obtained from the TTV modeling, within 1σ consistency.

4.2. Global Modeling: Transit+RV+RM effect

As the main result of this work, we present the joint model TESS transit, HIRES radial velocities, and NEID RM-effect signals to derive the planetary and orbital properties of TOI-2145b. We use the `exoplanet` package (D. Foreman-Mackey et al. 2019, 2021) to build the model and perform the Markov Chain Monte Carlo (MCMC) using the `PyMC` package (A.-P. Oriol et al. 2023).

We run three different models, all including TESS and HIRES data, but one with the RM-effect signal reduced by `NEID-DRP`, one by `SERVAL`, and one by DT. The model includes the following planetary and orbital parameters:

1. P: orbital period;
2. T_C: reference transit epoch;
3. b: impact parameter;
4. $R_p/R_\star$: planet-to-star radius ratio;
5. M_p: planet mass;
6. e: orbital eccentricity;
7. ω: argument of periapse;
8. λ: projected stellar obliquity.

Among these free parameters, a uniform prior is used on P, T_C, b, and λ, a log-uniform prior is used on $R_p/R_\star$ and M_p, and a unit disk vector is used on $\sqrt{e}\cos\omega$ and $\sqrt{e}\sin\omega$, where both e and ω are uniformly distributed. For both the `NEID-DRP` and `SERVAL` fittings, we use the T. Hirano et al. (2011) model to calculate the RV anomaly due to the RM effect. In addition to the quadratic limb-darkening coefficients (D. M. Kipping 2013) for the TESS transits, we model another pair for the NEID observations. Additionally, we model RV jitters, $\sigma_{\rm RV,\ DRP}$ and $\sigma_{\rm RV,\ SERVAL}$, in log-uniform space as free parameters added to both HIRES and NEID RV uncertainties. Lastly, we model the projected stellar rotation velocity $v \sin i_\star$ using a normal prior derived from the spectra. Independently, we perform the joint modeling of the TESS transit, HIRES RV, and NEID DT signals. We model the planetary shadow at each time snapshot as a Gaussian profile that is broadened by the instrumental resolution and macroturbulence of the host star $v_{\rm marco}$, which follows a prior uniformly between 0 and 10 km s^{-1}. The center of the velocity profile depends on the projected stellar obliquity λ and will be inferred. For each model, we begin with an optimization and then run the MCMC with 5000 tuning steps and 3000 draws with four independent chains. To check the convergence and sampling efficiency, we use the Gelman–Rubin diagnostic ($\hat{\mathcal{R}}$ convergence to 1; A. Gelman & D. B. Rubin 1992) and the effective sample size (A. Gelman et al. 2014). All three models have passed the convergence test. A summary of the results can be found in Table 1 and Figures 2 and 3.

The `NEID-DRP` and `SERVAL` pipelines infer $\lambda = 9.0^{+15.6}_{-13.4}{}^\circ$ and $\lambda = 10.9^{+11.8}_{-11.5}{}^\circ$, respectively, while the DT signal infers

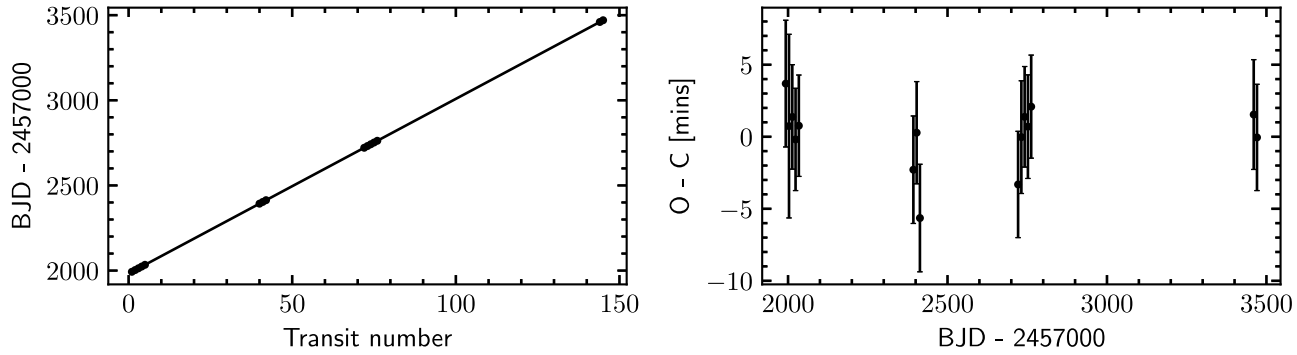

Figure 1. TTV on TOI-2145b. The planet exhibits a TTV of less than 5 minutes over a 4 yr baseline, with a typical midtransit time uncertainty of 2.7 minutes.

Table 1
Median Values and 68% Highest Density Intervals for the Stellar and Planetary Parameters of the TOI-2145 (TIC-88992642) System

Parameter	Units	Values		
Stellar Properties				
α_{J2016}	Gaia DR3 RA (HH:MM:SS.ss)	17:35:01.94		
δ_{J2016}	Gaia DR3 Dec (DD:MM:SS.ss)	+40:41:42.15		
ϖ	Gaia DR3 parallax (mas)	4.420 ± 0.013		
G	Gaia DR3 G magnitude	8.9453		
G_{BP}	Gaia DR3 G_{BP} magnitude	9.2178		
G_{RP}	Gaia DR3 G_{RP} magnitude	8.5075		
$M_\star$	Stellar mass ($M_\odot$)	1.71 ± 0.04		
$R_\star$	Stellar radius ($R_\odot$)	$2.75^{+0.06}_{-0.05}$		
$\rho_\star$	Stellar density ($\rho_\odot$)	0.081 ± 0.005		
$\log g$	Stellar surface gravity (cgs)	3.79 ± 0.02		
$T_{\rm eff}$	Stellar effective temperature (K)	6206^{+81}_{-75}		
[m/H]	Stellar bulk metallicity (dex)	$+0.28^{+0.06}_{-0.05}$		
Age	Stellar age (Gyr)	$1.6^{+0.2}_{-0.1}$		
$v \sin i_{\star,\ \rm spec}$	Spectral projected line broadening (km s^{-1})	ˇsin i		
Planetary and Orbital Properties				
		With DT	With SERVAL	With NEID-DRP
P	Period (days)	$10.261128^{+0.000009}_{-0.000007}$	$10.261132^{+0.000008}_{-0.000008}$	$10.261131^{+0.000008}_{-0.000008}$
T_C	Midtransit time (BJD-2457000)	$1982.49662^{+0.00055}_{-0.00054}$	$1982.49655^{+0.00053}_{-0.00055}$	$1982.49656^{+0.00052}_{-0.00054}$
a	Semimajor axis (au)	$0.1117^{+0.0035}_{-0.0034}$	$0.1095^{+0.0030}_{-0.0033}$	$0.1098^{+0.0035}_{-0.0031}$
$a/R_\star$	Planet–star separation	$8.74^{+0.16}_{-0.14}$	$8.58^{+0.14}_{-0.13}$	$8.60^{+0.17}_{-0.15}$
b	Impact parameter	$0.165^{+0.069}_{-0.082}$	$0.168^{+0.108}_{-0.104}$	$0.192^{+0.124}_{-0.106}$
i	Orbital inclination (°)	$88.6^{+0.7}_{-0.6}$	$88.6^{+1.1}_{-0.7}$	$88.4^{+1.0}_{-1.0}$
$R_p/R_\star$	Planet–star radius ratio	$0.04082^{+0.00024}_{-0.00027}$	$0.04099^{+0.00026}_{-0.00029}$	$0.04101^{+0.00029}_{-0.00029}$
R_p	Planet radius ($R_{\rm Jup}$)	$1.092^{+0.030}_{-0.028}$	$1.097^{+0.028}_{-0.026}$	$1.098^{+0.026}_{-0.028}$
M_p	Planet mass ($M_{\rm Jup}$)	$5.68^{+0.37}_{-0.34}$	$5.51^{+0.31}_{-0.35}$	$5.52^{+0.35}_{-0.34}$
e	Orbital eccentricity	$0.214^{+0.014}_{-0.014}$	$0.230^{+0.011}_{-0.012}$	$0.224^{+0.013}_{-0.013}$
ω	Argument of periapse (°)	$96.2^{+2.4}_{-2.5}$	$95.9^{+2.4}_{-2.4}$	$96.0^{+2.4}_{-2.3}$
λ	Projected stellar obliquity (°)	$6.8^{+2.9}_{-3.8}$	$10.9^{+11.8}_{-11.5}$	$9.0^{+15.6}_{-13.4}$
Other Parameters in the Joint Model				
$v \sin i_\star$	Fitted projected line broadening (km s^{-1})	$18.06^{+0.36}_{-0.39}$	$18.61^{+0.78}_{-0.95}$	$18.39^{+0.94}_{-0.88}$
$\sigma_{\rm RV,\ HIRES}$	HIRES RV jitter (m s^{-1})	$23.2^{+2.3}_{-2.8}$	$23.5^{+2.4}_{-2.7}$	$23.3^{+2.5}_{-2.7}$
$v_{\rm macro,\ v1}$	Host star macroturbulence, visit 1 (km s^{-1})	$2.64^{+0.20}_{-0.23}$	…	…
$v_{\rm macro,\ v2}$	Host star macroturbulence, visit 2 (km s^{-1})	$2.34^{+0.20}_{-0.21}$	…	…
$\sigma_{\rm RV,\ SERVAL,\ v1}$	SERVAL RV jitter, visit 1 (m s^{-1})	…	$5.9^{+1.6}_{-2.0}$	…
$\sigma_{\rm RV,\ SERVAL,\ v2}$	SERVAL RV jitter, visit 2 (m s^{-1})	…	$4.8^{+1.3}_{-1.3}$	…
$\sigma_{\rm RV,\ DRP,\ v1}$	NEID-DRP RV jitter, visit 1 (m s^{-1})	…	…	$8.4^{+2.3}_{-2.7}$
$\sigma_{\rm RV,\ DRP,\ v2}$	NEID-DRP RV jitter, visit 2 (m s^{-1})	…	…	$6.1^{+1.6}_{-2.1}$

Note. The planetary and orbital parameters are derived from a joint fit of TESS transits, HIRES, and NEID radial velocities. Gaia magnitudes and spectral line broadening parameter are obtained from the Gaia Data Release 3 (Gaia Collaboration et al. 2021). Both NEID RM-effect observations are included in the joint fit. Planetary parameters inferred from the DT signal are used for discussion.

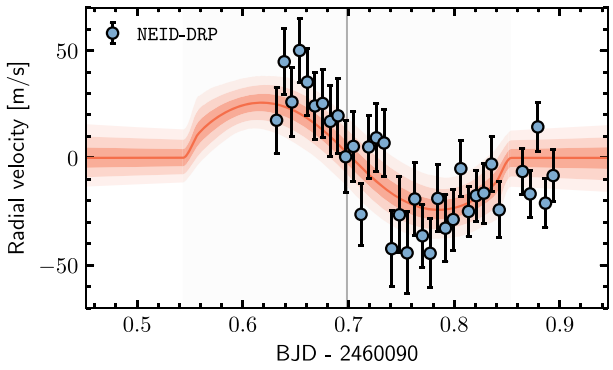

(a) In-transit RVs reduced by the NEID-DRP v1.3.0 pipeline, which infer $\lambda = 9.0^{+15.6}_{-13.4}{}^{\circ}$. The orbit trend has been subtracted.

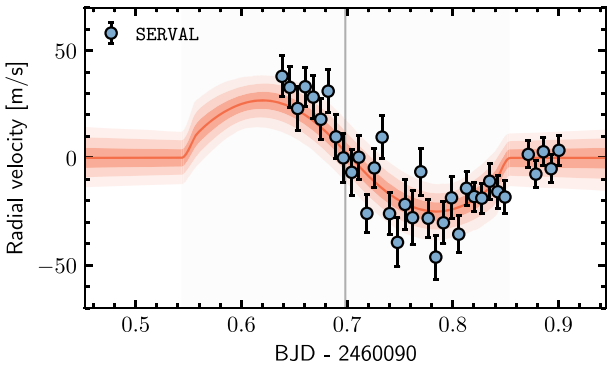

(b) In-transit RVs reduced by the SERVAL pipeline, which infer $\lambda = 10.9^{+11.8}_{-11.5}{}^{\circ}$. The orbit trend has been subtracted.

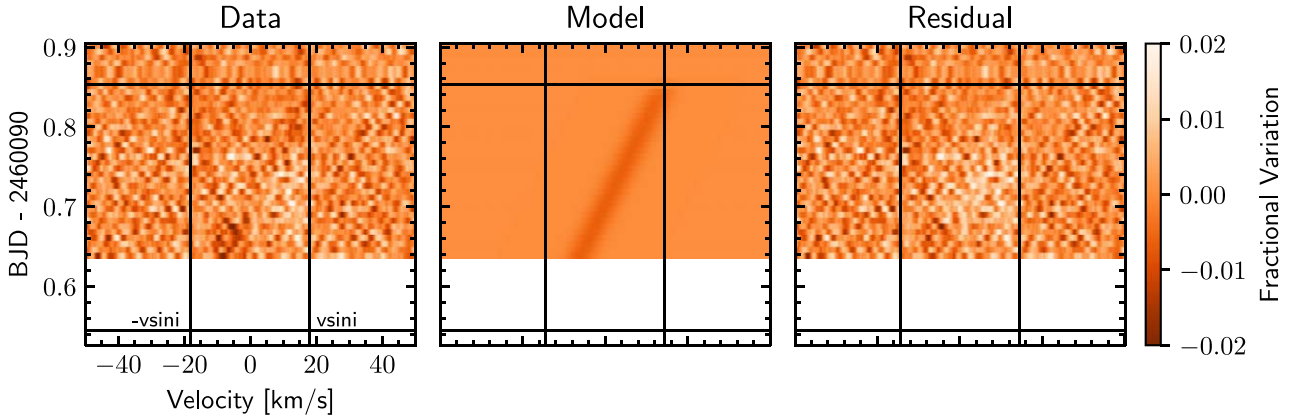

(c) Doppler Tomography signal, which infers $\lambda = 6.8^{+2.9}_{-3.8}{}^{\circ}$.

Figure 2. NEID's first RM-effect visit on 2023 May 26. Data were reduced by three different reduction techniques. The inferred projected stellar obliquities are consistent, but DT provides the tightest constraint. (a) and (b) In-transit RV measurements of the TOI-2145 system using the NEID spectra. The blue dots and black bars are NEID RVs and their corresponding uncertainties. The planet's transit and midtransit time are indicated by the gray shaded region and gray vertical line, respectively. (c) The DT (planetary shadow) signal of the TOI-2145 system during TOI-2145b's transit. The left, middle, and right panels are data extracted from the NEID spectra, best-fit model, and the residual of the data after subtracting the best-fit model, respectively. The color scale presents the flux variation of the velocity channel.

$\lambda = 6.8^{+2.9}_{-3.8}{}^{\circ}$. The three inferred projected stellar obliquities are consistent with each other, ruling out a polar or retrograde orbit of TOI-2145b. Because of the high dimensionality of the DT signal, the DT model provides the tightest constraint on the projected stellar obliquity λ. We adopt the DT results for the discussion of this work.

In summary, TOI-2145b is a $5.68^{+0.37}_{-0.34}\,M_{\rm Jup}$ planet on a moderately eccentric ($e_p = 0.214^{+0.014}_{-0.014}$), slightly misaligned ($\lambda = 6.8^{+2.9}_{-3.8}{}^{\circ}$) orbit. The planet's orbital period is $P = 10.261128^{+0.000009}_{-0.000007}$ day, with a semimajor axis of $a = 0.1117^{+0.0035}_{-0.0034}$ au and a planet–star separation of $a/R_\star = 8.74^{+0.16}_{-0.14}$. The planet has a size of $R_p = 1.092^{+0.030}_{-0.028}\,R_{\rm Jup}$. The planet's mass, eccentricity, and radius are consistent with previous estimates (J. E. Rodriguez et al. 2023; A. Chontos et al. 2024).

In all three models, the HIRES RVs present high RV jitters in residuals, with an amplitude of $23\,{\rm m\,s^{-1}}$. We use the Gaussian process kernels for granulation and oscillations given in J. K. Luhn et al. (2023) to estimate the expected white-noise-equivalent levels of additional variability due to granulation and oscillations. The granulation kernel is composed of two Harvey-like components with frequencies and amplitudes scaled by the effective temperature of 6206^{+81}_{-75} K and $\log g$ of 3.79 ± 0.02; the expected white-noise equivalent for granulation is $1.6\,{\rm m\,s^{-1}}$. The oscillation kernel is described by a stochastically driven, damped harmonic oscillator with frequency and amplitude scaled by $\nu_{\rm max}$; the expected white-noise equivalent for oscillations is $1.7\,{\rm m\,s^{-1}}$. The large RV jitters are likely due to the high $v \sin i_\star$ of the host star, which is $\sim 18\,{\rm km\,s^{-1}}$.

4.3. Search for External Companions

Next, we search for additional planets or stellar companions in the TOI-2145 system. Given TOI-2145b's high mass and eccentric orbit, its external perturbers could potentially be massive. Despite the long baseline of HIRES RVs, we find no clear evidence of additional companions in the RV residuals due to the large RV jitters caused by the fast rotation of the host star. The median RV residual is at a level of $12\,{\rm m\,s^{-1}}$, while the RV jitter combined with HIRES measurement uncertainty is about $24\,{\rm m\,s^{-1}}$.

The proper motion anomaly (PMa) technique is a powerful approach for searching for long-period, massive companions orbiting TOI-2145. This technique is based on identifying the difference between the long-term proper motion of the star, as measured by Gaia and Hipparcos, and the short-term proper

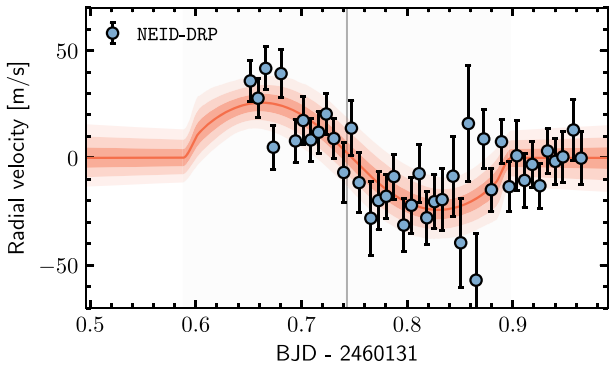

(a) In-transit RVs reduced by the NEID-DRP v1.3.0 pipeline, which infer $\lambda = 9.0^{+15.6}_{-13.4}{}^{\circ}$. The orbit trend has been subtracted.

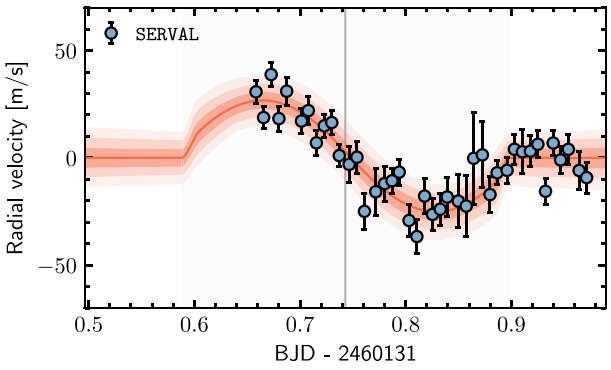

(b) In-transit RVs reduced by the SERVAL pipeline, which infer $\lambda = 10.9^{+11.8}_{-11.5}{}^{\circ}$. The orbit trend has been subtracted.

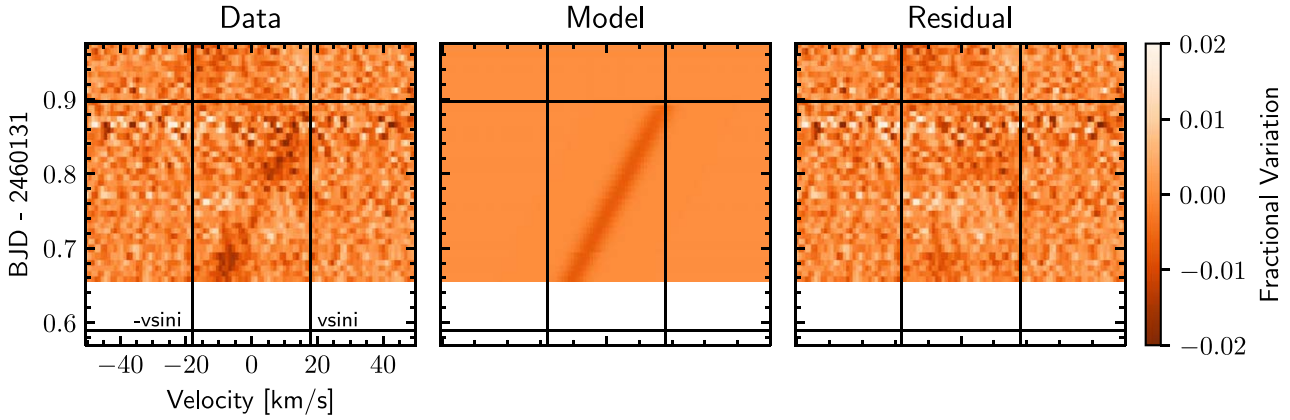

(c) Doppler Tomography signal, which infers $\lambda = 6.8^{+2.9}_{-3.8}{}^{\circ}$.

Figure 3. Same as Figure 2 but for the NEID's second RM-effect visit on 2023 July 6.

motion recorded by Gaia alone (T. D. Brandt 2021; P. Kervella et al. 2022). The anomaly could indicate the presence of an external companion, though it is subject to degeneracy in mass and semimajor axis. We adopt the PMa for TOI-2145 (HIP 86040; Gaia DR3 1344163891352965632) from the P. Kervella et al. (2022) catalog. The star exhibits a tangential velocity anomaly of $66.5 \pm 44.8\ \mathrm{m\ s^{-1}}$. While the signal is insignificant, if the velocity anomaly of the star is indeed introduced by another planet, it could correspond to a $9 \pm 5\ M_{\mathrm{Jup}}$-mass planet at 5 au with mass–semimajor axis degeneracy. However, the contributions from stellar noise and instrumental systematics are not well understood, and thus the detection of the companion is inconclusive. Gaia DR4 may provide more evidence of the existence of external companions.

We also check if TOI-2145 has a common proper motion with any other stars from the P. Kervella et al. (2022) catalog. While a nearby star with a projected linear separation of 47100 au and a V-band magnitude of 15.9 is found, it receives a candidate companion score (P_{tot}) of 0.112 (see Section 3.4.3 of P. Kervella et al. 2022 for a detailed description of the metrics), indicating a low probability of being a comoving or bound companion. The star is likely a nearby field star.

5. Discussion

TOI-2145b is a 10.26 day, 5.7 ± 0.3 Jupiter-mass planet orbiting an evolved A-star. The planet has a moderately eccentric orbit of $e = 0.21 \pm 0.01$. In this work, we combine TESS and previous HIRES observations (A. Chontos et al. 2024) with our new NEID RM-effect measurements to constrain the planet's orbital properties. We find that TOI-2145b has a nearly aligned orbit with a projected stellar obliquity of $\lambda = 6.8^{+2.9}_{-3.8}{}^{\circ}$. Given the current low orbital eccentricity of TOI-2145b, the planet is unlikely to be undergoing high-eccentricity tidal migration unless it can excite its eccentricity to much higher values, for example, through secular interactions with other planets (C. Petrovich & S. Tremaine 2016). TOI-2145b more likely migrated inward from the outer disk or formed in situ. The observed orbital eccentricity and inclination of TOI-2145b are likely an outcome of the planet–disk interactions (P. C. Duffell & E. Chiang 2015) or postformation dynamical evolution with other planets in the system.

The TOI-2145 system is interesting from multiple perspectives. First, TOI-2145b is a super Jupiter, a class of giant planets with masses beyond $\sim 2\ M_{\mathrm{Jup}}$ but still below the brown dwarf's deuterium fusion limit. Recently, A. F. Gupta et al. (2024) showed that these super Jupiters tend to have more eccentric orbits than their less massive counterparts, potentially as a result of planet–planet interactions. Thus, it is interesting to understand whether TOI-2145b is born with this mass or grows due to collisions. Second, TOI-2145b's orbit is nearly aligned with its host star spin axis. We discuss how spin–orbit coupling may play a role in the planet's orbital obliquity. Third, TOI-2145b's host star is evolved. Because of the inflation of the host star radius, its planet–star separation ($a/R_{\star}$) decreased by a factor of 2 from roughly 18 to 9. The inflation of the star could potentially increase the planet–star tidal interactions, speeding

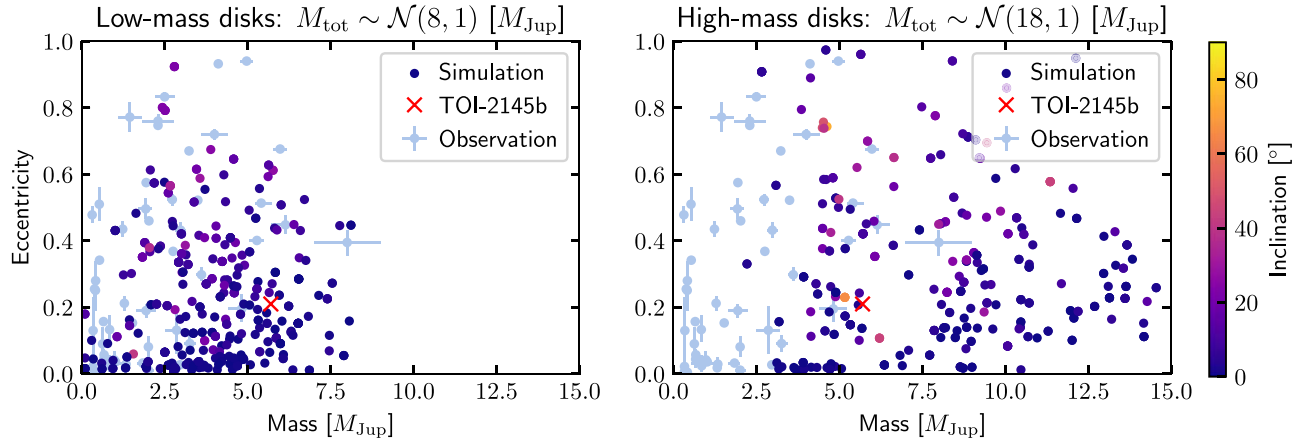

Figure 4. Mass and orbital properties of the innermost warm Jupiter in low-disk-mass and high-disk-mass scenarios. TOI-2145b is labeled as a red cross. Both planets born in a low-mass disk followed by collisions and in a high-mass disk followed by scatterings could explain the current properties of TOI-2145b.

up the spin–orbit alignment or heating the atmosphere of TOI-2145b. However, we do not see an inflation of TOI-2145b's radius, likely due to the high surface gravity of the planet and also the relatively short timescale since the star evolved off the main sequence.

5.1. Origins of Super Jupiters

TOI-2145b is noteworthy for its substantial mass. As a super Jupiter with nearly 6 times the mass of Jupiter, it raises the question: was it born with such a high mass, or did the planet acquire its mass through collisions between multiple planets? The observed positive mass–eccentricity relationship among warm giant planets (A. F. Gupta et al. 2024) may suggest the latter scenario, especially when considering TOI-2145b within a population of warm Jupiters.

Confirming this hypothesis requires a detailed, population-level dynamical study. Here, we build toy models with *N*-body simulations to explore two formation scenarios. We consider a four-planet system with the innermost planet having a semimajor axis of 0.1 au. While our understanding of the multiplicity of giant planets remains largely incomplete, RV surveys, such as the California Legacy Survey (L. J. Rosenthal et al. 2021), suggest that a significant fraction (∼40%) of giant planets are in multiplanet systems (W. Zhu 2022). Moreover, the four-planet setup facilitates the formation of super Jupiters through collisions between Jupiter-mass objects.

To construct the initial condition of a planetary system, we use three free parameters: the total mass of the four planets ($M_{\rm tot}$), the standard deviation of mass distribution among the four planets in the same system (σ_{m_p}), and the mutual Hill radii between neighboring planet pairs (Δa_p). The masses of the planets in the same system are drawn from a normal distribution with a mean of $M_{\rm tot}/4$ and a variance of σ_{m_p}. The initial eccentricity and inclination are assumed to be 0.01 for all planets. In all population synthesis simulations presented in this work, we assume σ_{m_p} follows a normal distribution with a mean of 1 and a standard deviation of 0.5 in the unit of Jupiter mass, bounded between 0 and 2. Δa_p follows a normal distribution with a mean of 4 and a standard deviation of 0.2. We vary the $M_{\rm tot}$ to explore how it determines the outcome of the planetary system architecture.

We consider a low-disk-mass scenario with a total planet mass $M_{\rm tot}$ following $\mathcal{N}(8, 1)$ and a high-disk-mass scenario with $M_{\rm tot} \sim \mathcal{N}(18, 1)$, both in units of Jupiter mass. We note that the definitions of low and high disk mass here are relative to each other in two scenarios. We simulate each system for 10 Myr using `REBOUND` with the `IAS15` integrator (H. Rein & S. F. Liu 2012; H. Rein & D. S. Spiegel 2015). Collisions are checked at each timestep for crossing pathways using the `line` algorithm and resolved using the `merge` module, which conserves mass, momentum, and volume but not energy. The realization of mass, orbital eccentricity, and inclination for the innermost warm Jupiter is shown in Figure 4. TOI-2145b is indicated by a red cross. Observed warm Jupiters are plotted in blue dots for reference.

For the low-disk-mass case, as shown in the left panel of Figure 4, massive planets above 5 Jupiter masses are mostly grown through collisions, as is the case for TOI-2145b. These planets first have their eccentricities excited by interactions with other planets in the system, including scattering and ejection. Later on, collisions happen and tend to reduce the eccentricity of the planets. Planets between 2 and 5 Jupiter masses are also in systems with significant scattering and ejection and thus experience eccentricity excitation. However, they have fewer mergers than those above 5 Jupiter masses. Planets below 2 Jupiter masses typically have low eccentricities; those with higher eccentricities are often dynamically unstable and get ejected. Collisions with the host star are rare. For the high-disk-mass case, as shown in the right panel of Figure 4, massive planets are more common. For planets with a mass similar to TOI-2145b, scattering and ejection are still the dominant dynamical mechanisms to excite their eccentricities. Collisions, however, happen less frequently to these planets in the high-disk-mass case than in the low-disk-mass case. Therefore, super Jupiters born in low-mass disks and formed via collision are expected, on average, to have lower eccentricities than those born massive. A similar trend is observed in the inclination distribution, although it is less pronounced.

As shown by our simulations, TOI-2145b can be reproduced in both formation scenarios. It is plausible for the planet to form from a low disk mass followed by collisions or from a massive disk with little or no collision. However, the two proposed scenarios for the formation of super Jupiters lead to distinct predictions about the overall eccentricity distribution of super Jupiters: super Jupiters born massive tend to have a broader eccentricity distribution than super Jupiters grown out of collisions. Based on existing observations of warm Jupiters,

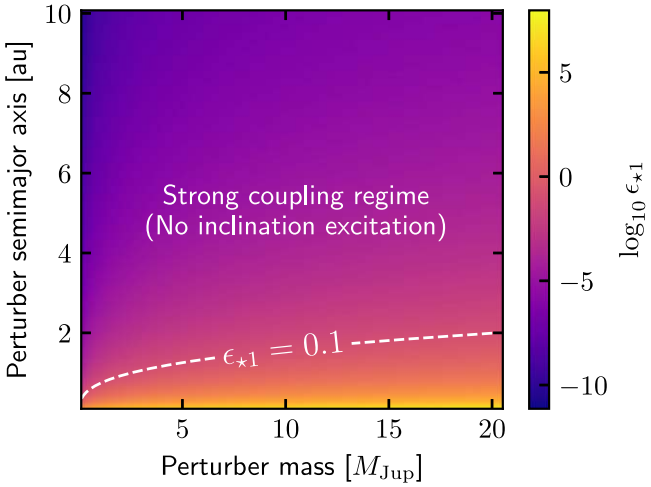

Figure 5. Spin–orbit coupling factor $\epsilon_{\star 1}$ between TOI-2145 and TOI-2145b given different perturber properties. Here, we assume a stellar rotation rate of 5 days. The dashed line corresponds to $\epsilon_{\star 1} = 0.1$. Perturbers above the line are unlikely to excite the mutual inclination of the inner planet due to spin–orbit coupling.

shown as blue dots in Figure 4, the collision scenario could provide a better match to the data. Additionally, our simulations show that super Jupiters formed through collisions are generally expected to have companions with masses similar to or lower than those of regular Jupiters, whereas those born with inherently high masses are likely to have companions with comparable masses. Consequently, searching for companion planets could be important in understanding the mass distribution within the system and determining which formation scenario is more plausible. This trend is based on the assumption of initial mass similarity among the planets, which will need to be examined in the future.

5.2. Spin–Orbit Coupling of Close-in Planets

TOI-2145b has joined the group of about two dozen warm Jupiters that have spin–orbit measurements, many of which show a tendency toward spin–orbit alignment around single stars (e.g., J. Dong et al. 2022; M. Rice et al. 2022; J. I. Espinoza-Retamal et al. 2023; A. Bieryla et al. 2024; B. T. Radzom et al. 2024; X.-Y. Wang et al. 2024). It is unclear if such a trend persists in binary systems. For example, TOI-1859b is a 64 day warm Jupiter with an eccentric and misaligned orbit ($e = 0.57^{+0.12}_{-0.16}$, $\lambda = 38.9^{+2.8}_{-2.7}$°), whose host star has a distant companion (J. Dong et al. 2023). The role of the binary companion in determining planet formation remains open for discussion. Here, we discuss the importance of spin–orbit coupling and how it might affect stellar obliquity distribution. The gravitational coupling between the close-in giant planet and its oblate host star may prevent the spin–orbit misalignment of the giant planet's orbit excited by the companion. Under the assumption that the dynamical perturbation of warm Jupiters happens mostly after they migrate at the current orbital distances, the external companion needs to overcome spin–orbit coupling from the star to excite the inner planet's inclination. Such an effect is the strongest around the fast rotating host stars, which could be TOI-2145 in this case. D. Lai et al. (2018) defined the planet–star coupling factor $\epsilon_{\star 1}$, where the smaller the value, the stronger the coupling between the planet and the star, and the weaker the more distant, external perturber to excite the inclination of the planet. Using Equation (24) in D. Lai et al. (2018), the planet–star coupling factor $\epsilon_{\star 1}$ follows

$$\epsilon_{\star 1} = \frac{\omega_{12}}{\omega_{\star 1}}\left(\frac{1-\omega_{\star 2}/\omega_{12}}{1+S_\star/L_1}\right) \simeq 1.25\left(\frac{6k_{q\star}}{k_\star}\right)^{-1}\frac{m_2}{m_1}\left(\frac{a_1}{0.04\ \mathrm{au}}\right)^{9/2}\left(\frac{\tilde{a}_2}{1\ \mathrm{au}}\right)^{-3}\left(\frac{P_\star}{30\ \mathrm{day}}\right) \times \left(\frac{M_\star}{M_\odot}\right)^{1/2}\left(\frac{R_\star}{R_\odot}\right)^{-3}\left(\frac{1}{1+S_\star/L_1}\right), \quad (1)$$

where $S_\star/L_1$ is the ratio of stellar spin angular momentum and orbital angular momentum of the inner planet,

$$\frac{S_\star}{L_1} = 0.079\left(\frac{k_\star}{0.06}\right)^{-1}\left(\frac{m_1}{M_J}\right)^{-1}\left(\frac{a_1}{0.04\ \mathrm{au}}\right)^{-1/2}\left(\frac{P_\star}{30\ \mathrm{day}}\right)^{-1} \times \left(\frac{M_\star}{M_\odot}\right)^{1/2}\left(\frac{R_\star}{R_\odot}\right)^{2}. \quad (2)$$

Here, the notation $\star$ means the central star, 1 means the inner planet, and 2 means the distant perturber. ω_{xy} means the precession rate of x due to y. $k_{q\star}$ and $k_\star$ are the Love numbers of the star and the planet, m_1 and m_2 are the masses of the planet and the perturber, respectively, a_1 is the planet's semimajor axis, $\tilde{a}_2$ is the perturber's effective semimajor axis $\tilde{a}_2 = a_2\sqrt{1-e_2^2}$, $P_\star$ is the star's rotation period, and $M_\star$ and $R_\star$ are the star's mass and radius, respectively.

In Figure 5, we show how the star–planet coupling factor, $\epsilon_{\star 1}$, varies for a perturber with different masses and semimajor axes. If $\epsilon_{\star 1} \ll 1$, we consider the star–planet coupling is strong, and thus it is unlikely that the perturber will excite the inclination of the close-in giant planet. As shown in Figure 5, for a perturber with a semimajor axis greater than ~1–2 au, no matter of its mass, regardless of its mass, the inner planet is always in the strong spin–orbit coupling regime with the star, resulting in a consistently low stellar obliquity. For example, the hypothetical planet with a semimajor axis of 5 au and a mass of 9 $M_{\rm Jup}$ inferred from the Gaia and Hipparcos PMas would be too distant from TOI-2145b to excite its inclination. If the perturber is close in ($a_2 \lesssim 1$ au), it may overcome the gravitational coupling. Although this is not indicated by the current stellar obliquity measurements, the existence of such a perturber could potentially be detected in long-term RV observations. However, the RV precision might be compromised due to the star's high $v \sin i_\star$.

5.3. Stellar Obliquity of Evolved Stars

The RM-effect observation around evolved stars is challenging due to the increased transit duration caused by stellar radius inflation. Notably, TOI-2145b has the longest orbital period among planets orbiting evolved stars for which an RM-effect measurement has been obtained. It joins a small population of planets, including WASP-71b (A. M. S. Smith et al. 2013; D. J. A. Brown et al. 2017), HAT-P-7b (N. Narita et al. 2009; J. N. Winn et al. 2009; S. Albrecht et al. 2012; M. N. Lund et al. 2014), TOI-1181b (N. Saunders et al. 2024), TOI-4379b (N. Saunders et al. 2024), and TOI-6029b

(N. Saunders et al. 2024). These planets have orbital periods ranging from 2 to 6 days and masses of a few Jupiter masses. Most of these planets, except HAT-P-7b, indicate a low stellar obliquity.

TOI-2145 is a hot star that had an effective temperature near or above the Kraft break before becoming a subgiant. While stellar evolution may decrease the planet–star separation ($a/R_\star$), thereby increasing star–planet interactions and speeding up the tidal realignment process, whether the planet had a spin–orbit misalignment before stellar evolution remains open for discussion. As discussed in the previous subsection, spin–orbit coupling between the star and the planet may prevent the excitation of TOI-2145b's mutual inclination relative to the perturber planet in the first place.

Acknowledgments

We appreciate the referee for a thoughtful and detailed report, which helped us improve our paper. We thank Zhao Guo for the insightful discussions about the detectability of asteroseismology signals. We appreciate the fruitful discussion with Phil Armitage on the origins of super Jupiters and sub-Saturns. We would also like to thank Dong Lai for the insightful discussions about the spin–orbit coupling of close-in planets. Special thanks to Te Han for the development and discussions about the NEID `SpecMatch`. We extend our gratitude to the Flatiron CCA and the NYC astronomical community, as well as to Nora Eisner, Lehman Garrison, Isabel Colman, Lily Zhao, Quang Tran, and Julianne Dalcanton, for their support in the application of the Lomb–Scargle periodogram for stellar rotation periodicity detections. The Flatiron Institute is a division of the Simons foundation. S.W. acknowledges support from Heising–Simons Foundation grant #2023-4050 and support from the NASA Exoplanets Research Program NNH23ZDA001N-XRP (grant #80NSSC24K0153). This research was carried out, in part, at the Jet Propulsion Laboratory and the California Institute of Technology under a contract with the National Aeronautics and Space Administration. The Center for Exoplanets and Habitable Worlds is supported by the Pennsylvania State University and the Eberly College of Science.

This work includes data collected by the TESS mission, which are publicly available from the Mikulski Archive for Space Telescopes (MAST). Funding for the TESS mission is provided by the NASA Science Mission directorate. We acknowledge the use of public TESS data from pipelines at the TESS Science Office and at the TESS Science Processing Operations Center. Resources supporting this work were provided by the NASA High-End Computing (HEC) Program through the NASA Advanced Supercomputing (NAS) Division at Ames Research Center for the production of the SPOC data products. The TESS data presented in this paper were obtained from the MAST at the Space Telescope Science Institute. The specific observations analyzed can be accessed via the TESS all sectors Light Curves page (Team 2021a) and the TESS all sectors "Fast" Light Curves page (Team 2021b). The TESS Input Catalog and Candidate Target List can be accessed via its page (STScI 2018). This work has made use of data from the European Space Agency (ESA) mission Gaia (https://www.cosmos.esa.int/gaia), processed by the Gaia Data Processing and Analysis Consortium (DPAC; https://www.cosmos.esa.int/web/gaia/dpac/consortium).

Data presented were obtained by the NEID spectrograph built by Penn State University and operated at the WIYN Observatory by NOIRLab, under the NN-EXPLORE partnership of the National Aeronautics and Space Administration and the National Science Foundation. These results are based on observations obtained with NEID on the WIYN 3.5 m Telescope at KPNO (co-PIs: Ashley Chontos and Jiayin Dong, NOIRLab 2023A-652300). WIYN is a joint facility of the University of Wisconsin-Madison; Indiana University; NSF's NOIRLab; the Pennsylvania State University; Purdue University; University of California, Irvine; and the University of Missouri. The authors are honored to be permitted to conduct astronomical research on Iolkam Du'ag (Kitt Peak), a mountain with particular significance to the Tohono O'odham.

This research made use of `exoplanet` (D. Foreman-Mackey et al. 2019, 2021) and its dependencies (Astropy Collaboration et al. 2013, 2018; D. M. Kipping 2013; D. Foreman-Mackey et al. 2017, 2019; D. Foreman-Mackey 2018; R. Luger et al. 2019; E. Agol et al. 2020; T. Wiecki et al. 2022).

Facilities: TESS, Gaia, WIYN/NEID, Keck:I, Exoplanet Archive.

Software: `ArviZ` (R. Kumar et al. 2019), `astropy` (Astropy Collaboration et al. 2013, 2018), `celerite2` (D. Foreman-Mackey et al. 2017; D. Foreman-Mackey 2018), `exoplanet` (D. Foreman-Mackey et al. 2019, 2021), `Jupyter` (T. Kluyver et al. 2016), `Matplotlib` (J. D. Hunter 2007; M. Droettboom et al. 2016), `NumPy` (S. van der Walt et al. 2011; C. R. Harris et al. 2020), `pandas` (Wes McKinney 2010; pandas development team 2020), `PyMC` (T. Wiecki et al. 2022), `SciPy` (P. Virtanen et al. 2020), `Tapir` (E. Jensen 2013).

ORCID iDs

Jiayin Dong https://orcid.org/0000-0002-3610-6953
Ashley Chontos https://orcid.org/0000-0003-1125-2564
George Zhou https://orcid.org/0000-0002-4891-3517
Gudmundur Stefansson https://orcid.org/0000-0001-7409-5688
Songhu Wang https://orcid.org/0000-0002-7846-6981
Chelsea X. Huang https://orcid.org/0000-0003-0918-7484
Arvind F. Gupta https://orcid.org/0000-0002-5463-9980
Samuel Halverson https://orcid.org/0000-0003-1312-9391
Shubham Kanodia https://orcid.org/0000-0001-8401-4300
Jacob K. Luhn https://orcid.org/0000-0002-4927-9925
Suvrath Mahadevan https://orcid.org/0000-0001-9596-7983
Andrew Monson https://orcid.org/0000-0002-0048-2586
Jaime A. Alvarado-Montes https://orcid.org/0000-0003-0353-9741
Joe P. Ninan https://orcid.org/0000-0001-8720-5612
Paul Robertson https://orcid.org/0000-0003-0149-9678
Arpita Roy https://orcid.org/0000-0001-8127-5775
Christian Schwab https://orcid.org/0000-0002-4046-987X
Jason T. Wright https://orcid.org/0000-0001-6160-5888

References

Agol, E., Luger, R., & Foreman-Mackey, D. 2020, AJ, 159, 123
Albrecht, S., Winn, J. N., Johnson, J. A., et al. 2012, ApJ, 757, 18
Anderson, K. R., Lai, D., & Pu, B. 2020, MNRAS, 491, 1369
Astropy Collaboration, Price-Whelan, A. M., Sipőcz, B. M., et al. 2018, AJ, 156, 123
Astropy Collaboration, Robitaille, T. P., Tollerud, E. J., et al. 2013, A&A, 558, A33
Bieryla, A., Zhou, G., García-Mejía,, J., et al. 2024, MNRAS, 527, 10955
Boisse, I., Eggenberger, A., Santos, N. C., et al. 2010, A&A, 523, A88

Brandt, T. D. 2021, ApJS, 254, 42
Brown, D. J. A., Triaud, A. H. M. J., Doyle, A. P., et al. 2017, MNRAS, 464, 810
Butler, R. P., Wright, J. T., Marcy, G. W., et al. 2006, ApJ, 646, 505
Castelli, F., & Kurucz, R. L. 2004, in IAU Symp. 210, Modelling of Stellar Atmospheres, ed. N. Piskunov et al. (San Francisco, CA: ASP)
Chaplin, W. J., Cegla, H. M., Watson, C. A., Davies, G. R., & Ball, W. H. 2019, AJ, 157, 163
Chatterjee, S., Ford, E. B., Matsumura, S., & Rasio, F. A. 2008, ApJ, 686, 580
Choi, J., Dotter, A., Conroy, C., et al. 2016, ApJ, 823, 102
Chontos, A., Huber, D., Grunblatt, S. K., et al. 2024, arXiv:2402.07893
Collier Cameron, A., Guenther, E., Smalley, B., et al. 2010, MNRAS, 407, 507
Collins, K., Quinn, S. N., Latham, D. W., et al. 2018, AAS Meeting Abstracts, 231, 439.08
Donati, J.-F., Semel, M., Carter, B. D., Rees, D. E., & Cameron, A. C. 1997, MNRAS, 291, 658
Dong, J., Huang, C. X., Dawson, R. I., et al. 2021, ApJS, 255, 6
Dong, J., Huang, C. X., Zhou, G., et al. 2022, ApJL, 926, L7
Dong, J., Wang, S., Rice, M., et al. 2023, ApJL, 951, L29
Dotter, A. 2016, ApJS, 222, 8
Droettboom, M., Hunter, J., Caswell, T. A., et al. 2016, Matplotlib: Matplotlib v1.5.1, Zenodo, doi:10.5281/zenodo.44579
Duffell, P. C., & Chiang, E. 2015, ApJ, 812, 94
Espinoza-Retamal, J. I., Brahm, R., Petrovich, C., et al. 2023, ApJL, 958, L20
Ford, E. B., & Rasio, F. A. 2008, ApJ, 686, 621
Foreman-Mackey, D. 2018, RNAAS, 2, 31
Foreman-Mackey, D., Agol, E., Ambikasaran, S., & Angus, R. 2017, AJ, 154, 220
Foreman-Mackey, D., Czekala, I., Luger, R., et al. 2019, dfm/exoplanet: exoplanet v0.2.1, Zenodo, doi:10.5281/zenodo.3462740
Foreman-Mackey, D., Luger, R., Agol, E., et al. 2021, JOSS, 6, 3285
Frelikh, R., Jang, H., Murray-Clay, R. A., & Petrovich, C. 2019, ApJL, 884, L47
Gaia Collaboration, Brown, A. G. A., Vallenari, A., et al. 2021, A&A, 649, A1
Gelman, A., Carlin, J. B., Stern, H. S., et al. 2014, Bayesian Data Analysis (Boca Raton, FL: Chapman & Hall)
Gelman, A., & Rubin, D. B. 1992, StaSc, 7, 457
Gupta, A. F., Millholland, S. C., Im, H., et al. 2024, Natur, 632, 50
Halverson, S., Terrien, R., Mahadevan, S., et al. 2016, Proc. SPIE, 9908, 99086P
Harris, C. R., Jarrod Millman, K., van der Walt, S. J., et al. 2020, Natur, 585, 357
Hayward, T. L., Brandl, B., Pirger, B., et al. 2001, PASP, 113, 105
Henden, A. A., Levine, S., Terrell, D., & Welch, D. L. 2015, AAS Meeting Abstracts, 225, 336.16
Hirano, T., Suto, Y., Winn, J. N., et al. 2011, ApJ, 742, 69
Huang, C. X., Vanderburg, A., Pál, A., et al. 2020a, RNAAS, 4, 204
Huang, C. X., Vanderburg, A., Pál, A., et al. 2020b, RNAAS, 4, 206
Huber, D., Zinn, J., Bojsen-Hansen, M., et al. 2017, ApJ, 844, 102
Hunter, J. D. 2007, CSE, 9, 90
Jenkins, J. M., Twicken, J. D., McCauliff, S., et al. 2016, Proc. SPIE, 9913, 99133E
Jensen, E., 2013 Tapir: A Web Interface for Transit/Eclipse Observability, Astrophysics Source Code Library, ascl:1306.007
Jurić, M., & Tremaine, S. 2008, ApJ, 686, 603
Kanodia, S., Lin, A. S. J., Lubar, E., et al. 2023, AJ, 166, 105
Kanodia, S., Mahadevan, S., Ramsey, L. W., et al. 2018, Proc. SPIE, 10702, 107026Q
Kervella, P., Arenou, F., & Thévenin, F. 2022, A&A, 657, A7
Kipping, D. M. 2013, MNRAS, 435, 2152
Kluyver, T., Ragan-Kelley, B., Pérez, F., et al. 2016, in Positioning and Power in Academic Publishing: Players, Agents and Agendas, ed. F. Loizides & B. Scmidt (Amsterdam: IOS Press), 87
Kumar, R., Carroll, C., Hartikainen, A., & Martin, O. 2019, JOSS, 4, 1143
Lai, D., Anderson, K. R., & Pu, B. 2018, MNRAS, 475, 5231
Luger, R., Agol, E., Foreman-Mackey, D., et al. 2019, AJ, 157, 64
Luhn, J. K., Ford, E. B., Guo, Z., et al. 2023, AJ, 165, 98
Lund, M. N., Lundkvist, M., Silva Aguirre, V., et al. 2014, A&A, 570, A54
Narita, N., Sato, B., Hirano, T., & Tamura, M. 2009, PASJ, 61, L35
Oriol, A.-P., Virgile, A., Colin, C., et al. 2023, PeerJ Computer Science, 9, e1516
pandas development team 2020, pandas-dev/pandas: Pandas, v2.2.2, Zenodo, doi:10.5281/zenodo.3509134
Petigura, E. A. 2015, PhD thesis, Univ. California, Berkeley
Petrovich, C., & Tremaine, S. 2016, ApJ, 829, 132
Radzom, B. T., Dong, J., Rice, M., et al. 2024, AJ, 168, 116
Rein, H., & Liu, S. F. 2012, A&A, 537, A128
Rein, H., & Spiegel, D. S. 2015, MNRAS, 446, 1424
Rice, M., Wang, S., Wang, X.-Y., et al. 2022, AJ, 164, 104
Ricker, G. R., Winn, J. N., Vanderspek, R., et al. 2014, Proc. SPIE, 9143, 914320
Robertson, P., Anderson, T., Stefansson, G., et al. 2019, JATIS, 5, 015003
Rodriguez, J. E., Quinn, S. N., Vanderburg, A., et al. 2023, MNRAS, 521, 2765
Rosenthal, L. J., Fulton, B. J., Hirsch, L. A., et al. 2021, ApJS, 255, 8
Saunders, N., Grunblatt, S. K., Chontos, A., et al. 2024, AJ, 168, 81
Schwab, C., Rakich, A., Gong, Q., et al. 2016, Proc. SPIE, 9908, 99087H
Skrutskie, M. F., Cutri, R. M., Stiening, R., et al. 2006, AJ, 131, 1163
Smith, A. M. S., Anderson, D. R., Bouchy, F., et al. 2013, A&A, 552, A120
Stefansson, G., Hearty, F., Robertson, P., et al. 2016, ApJ, 833, 175
Stefànsson, G., Mahadevan, S., Petrovich, C., et al. 2022, ApJL, 931, L15
STScI 2018, TESS Input Catalog and Candidate Target List, STScI, doi:10.17909/FWDT-2X66
Swift, J. J., Bottom, M., Johnson, J. A., et al. 2015, JATIS, 1, 027002
Team, M. 2021a, TESS Light Curves—All Sectors, STScI/MAST, doi:10.17909/T9-NMC8-F686
Team, M. 2021b, TESS "Fast" Light Curves—All Sectors, STScI/MAST, doi:10.17909/T9-ST5G-3177
van der Walt, S., Colbert, S. C., & Varoquaux, G. 2011, CSE, 13, 22
Virtanen, P., Gommers, R., Oliphant, T. E., et al. 2020, NatMe, 17, 261
Vogt, S. S., Allen, S. L., Bigelow, B. C., et al. 1994, Proc. SPIE, 2198, 362
Wang, X.-Y., Rice, M., Wang, S., et al. 2024, ApJL, 973, L21
Wes McKinney 2010, in Proc. 9th Python in Science Conf., ed. S. van der Walt & J. Millman (Austin, TX: SciPy), 56
Wiecki, T., Salvatier, J., Patil, A., et al. 2022, pymc-devs/pymc:, v4.1.7, Zenodo, doi:10.5281/zenodo.7467113
Wilson, M. L., Eastman, J. D., Cornachione, M. A., et al. 2019, PASP, 131, 115001
Winn, J. N., Johnson, J. A., Albrecht, S., et al. 2009, ApJL, 703, L99
Wright, J. T., Upadhyay, S., Marcy, G. W., et al. 2009, ApJ, 693, 1084
Wu, D.-H., Rice, M., & Wang, S. 2023, AJ, 165, 171
Zechmeister, M., Reiners, A., Amado, P. J., et al. 2018, A&A, 609, A12
Zhu, W. 2022, AJ, 164, 5